THE ASTROPHYSICAL JOURNAL, 443:764–779, 1995 April 20

NEW MODEL ATMOSPHERES FOR VERY COOL WHITE DWARFS WITH MIXED H/He AND PURE He COMPOSITIONS

P. BERGERON,[1] D. SAUMON,[2,3] AND F. WESEMAEL[1]
Received 1994 July 21; accepted 1994 October 27

ABSTRACT

New model atmosphere calculations for very cool white dwarfs with mixed H/He and pure He compositions are presented. The hydrogen-rich models incorporate improved cross section calculations of the collision-induced absorption by molecular hydrogen due to collisions with H_2, H, and He. The effects associated with variations in the effective temperature ($4000 \leq T_{\rm eff} \leq 10{,}000$ K), the surface gravity ($7.5 \leq \log g \leq 9.5$), and the chemical composition [$0 \leq N({\rm He})/N({\rm H}) \leq 100$] are investigated. Results from earlier calculations are confirmed qualitatively, but a more detailed comparison reveals large quantitative deviations. Cool white dwarfs with mixed H/He chemical compositions are shown to be easily recognizable from their predicted strong infrared flux deficiency.

Pure helium model calculations are described as well. These include a modified version of the recently developed equation of state of D. Saumon and G. Chabrier. Nonideal effects brought about by various equations of state are explored in detail. For the purpose of this analysis, a model of pressure ionization based on an accurate description of the interactions in a mostly atomic helium fluid is developed. The effects of pressure ionization are shown to be the most important issue in the model calculations. A critical discussion of previous generations of pure helium model calculations is presented. Finally, broadband color indices are provided for the complete model grid.

Subject headings: atomic processes — molecular processes — stars: abundances — stars: atmospheres — white dwarfs

1. INTRODUCTION

The chemical composition of white dwarfs above 10,000 K can be derived from a detailed, yet straightforward ultraviolet and/or optical spectroscopic analysis of the hydrogen, helium, and metallic lines. In the coolest white dwarf atmospheres, however, both hydrogen and helium become spectroscopically invisible, and inferences about the main constituent of their atmospheres can only be drawn from an analysis of the observed energy distributions. Although considerable progress has been accomplished in studies of hot white dwarfs (see, e.g., Liebert 1991; Fontaine & Wesemael 1991; Koester 1991), the chemical compositions of cool white dwarfs are not well determined, and their spectral evolution is still poorly understood. The physical complexity of cool atmosphere modeling is, in large part, responsible for this situation.

For example, the predicted emergent fluxes of cool white dwarfs are sensitive to the assumed convective efficiency until $T_{\rm eff}$ reaches values below $\sim$8000 K, where convection becomes adiabatic (Bergeron, Wesemael, & Fontaine 1992). A more acute problem is the formation of molecular hydrogen in the coolest hydrogen-rich models ($T_{\rm eff} \lesssim 6000$ K); the collision-induced (also called pressure-induced) opacity of H_2 has been acknowledged repeatedly to be the major source of uncertainty in hydrogen-rich model calculations (Shipman 1977; Mould & Liebert 1978; Wickramasinghe, Allen, & Bessell 1982). Furthermore, previous calculations of hydrogen-rich models have always assumed an ideal gas and, as such, nonideal effects in the equation of state (EOS) have never been evaluated.

[1] Département de Physique, Université de Montréal, C.P. 6128, Succ. Centre-Ville, Montréal, Québec, Canada H3C 3J7.
E-mail: bergeron, wesemael@astro.umontreal.ca.
[2] Lunar and Planetary Laboratory, University of Arizona, Tucson, AZ 85721. E-mail: dsaumon@lpl.arizona.edu.
[3] Hubble Postdoctoral Fellow.

The physical properties of pure helium models are even more extreme. In the coolest atmospheres, the opacity is dominated by He^- free-free absorption and Rayleigh scattering by neutral helium. These opacities are considerably weaker than those of hydrogen; the atmospheric pressures and densities of pure helium atmospheres become so large that the ideal gas is no longer a valid approximation. Model atmosphere calculations with pure helium compositions which include nonideal effects are already available in the literature (see § 2). As we discuss below, however, recent developments in plasma physics indicate that these earlier models are obsolete. Moreover, pressure ionization of helium has always been treated very approximately. We show below that an improved treatment of this physical process is crucial to determine the ionization equilibrium and the relative importance of the dominant sources of opacity.

In this paper, we use new results of state-of-the art atomic, molecular, and plasma physics to improve the accuracy and ultimately remove some of the uncertainties inherent to the calculations of cool white dwarf atmospheres. In § 2, we present our hydrogen-rich model calculations with various H/He compositions; helium-dominated compositions are considered as well. Pure helium models are described in § 3, where nonideal effects in the EOS and the problem of pressure ionization are discussed in detail. Both sets of models are shown to be significantly different from, and improved upon, earlier generations of model calculations. In § 4, we provide broadband color indices for a subsample of our model grid.

2. MODEL ATMOSPHERES WITH MIXED H/He COMPOSITIONS

2.1. *Input Physics*

The framework of our model atmosphere code is described at length in Bergeron, Wesemael, & Fontaine (1991). These models are nongray, are in LTE, and include only hydrogen

and helium species. Energy transport by convection is treated within the mixing-length theory. As discussed above, the uncertainties brought about by the assumed parametrization of the mixing-length theory become negligible at temperatures below ~ 8000 K (Bergeron et al. 1992), and the predicted fluxes show only a weak dependence at $T_{\rm eff} = 10{,}000$ K, the hottest model temperature in our calculations. We adopt the so-called ML2 version of the mixing-length theory throughout, following the nomenclature of Fontaine, Villeneuve, & Wilson (1981). For the purpose of this analysis, the EOS and opacity sources have been modified substantially, and we discuss the changes below.

In the models presented in Bergeron et al. (1991), molecular hydrogen was not included in the EOS calculation since the main purpose of that analysis was to study the high Balmer line profiles in cool DA stars; these lines are important only at temperatures where the effects of molecular hydrogen on the atmospheric structure can be neglected ($T_{\rm eff} \gtrsim 6000$ K). Here, the EOS has been modified to include molecular hydrogen species of H_2, H_2^+, and H_3^+. As discussed by Saumon et al. (1994a; see also Lenzuni, Chernoff, & Salpeter 1991), even though the H_2^+ and H_3^+ concentrations are small, their presence affects significantly the abundance of the H^- ion which is a dominant source of opacity in cool, hydrogen-rich atmospheres. We first consider an ideal (noninteracting) gas and evaluate the nonideal effects in § 2.4. Additional information about our EOS is given in Saumon et al. (1994a).

We also take advantage of the improved treatment of the collision-induced absorption (CIA) by molecular hydrogen due to collisions with H_2, H, and He and discussed at length by Lenzuni et al. (1991); other hydrogen and helium continuum opacities have been updated from this work as well. These CIA coefficients are largely based on the important work of Borysow, Frommhold, & Moraldi (1989) and Borysow & Frommhold (1989, 1990, and references therein). In their treatment of the H_2-H_2 collision-induced opacity, Lenzuni et al. used the results of Borysow et al. (1985) to evaluate the contribution of the rototranslational (RT) transitions. However, as discussed by Zheng & Borysow (1995), these calculations are strictly valid for temperatures below 300 K and include only the $v = 0 \rightarrow 0$ transition, while at higher temperatures, the contributions from additional $\Delta v = 0$ transitions with larger values of v may become important. Zheng & Borysow have obtained new results for the RT band which can now be applied in the temperature range 600–7000 K; these also take into account all $\Delta v = 0$ transitions for $v = 0$, 1, 2, and 3. We have thus felt necessary to modify the CIA calculations of Lenzuni et al. to include these latest results.

The total H_2-H_2 collision-induced opacity is displayed in Figure 1 where we compare the results of Lenzuni et al. with our updated calculations for two illustrative temperatures. The latter results were obtained in the following way. In their study, Lenzuni et al. used the $v = 0 \rightarrow 1$ rotovibrational (RV) calculations of Borysow & Frommhold (1990). The individual contributions from this transition are displayed in Figure 1 as well and have been calculated using computer codes generously supplied to us by Borysow and Frommhold. The results of Figure 1 indicate that for frequencies around ~ 6000 cm^{-1}, the $v = 0 \rightarrow 1$ RV band dominates the collision-induced opacity in the Lenzuni et al. calculations (this is also verified at all temperatures). In particular, there is no contribution at that frequency from the overtones and double vibrational RV transitions introduced by Lenzuni et al., *or* from the RT transitions. We have thus assumed that the contribution of the RV bands can be represented by the results of Lenzuni et al. for frequencies larger than 6000 cm^{-1} and by the $v = 0 \rightarrow 1$ RV calculations of Borysow & Frommhold (1990) for lower frequencies. The total opacity is then simply obtained by summing the contribution of the RV transitions with the results of Zheng & Borysow (1994) for the RT transitions. The latter have been calculated with codes kindly provided by these authors, and the individual contributions of this opacity are illustrated in Figure 1. At $T = 3000$ K, the new opacities exhibit an enhanced contribution of the RT band only in the

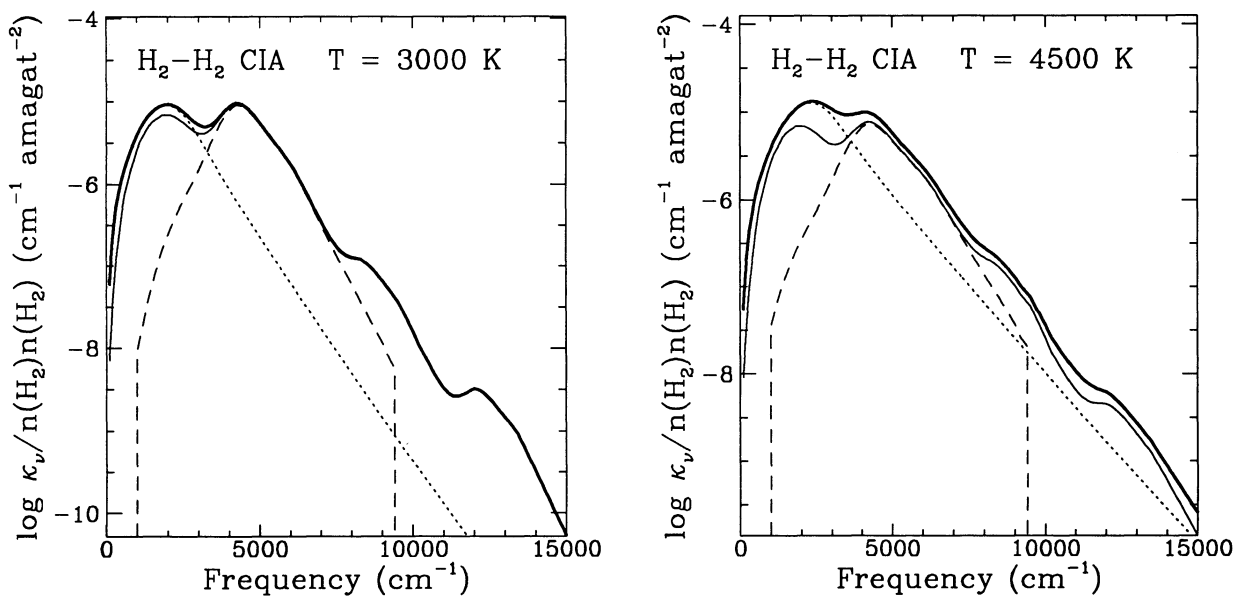

FIG. 1.—H_2-H_2 collision-induced opacity for two illustrative temperatures. The thin solid lines represent the results of Lenzuni et al. (1991), while the thick solid lines indicate our calculations updated with the new results of Zheng & Borysow (1995) for the rototranslational transitions (*dotted lines*). The individual contribution from the $v = 0 \rightarrow 1$ rotovibrational transitions are shown as dashed lines.

far-infrared ($\lambda \lesssim 3$ μm) with respect to the calculations of Lenzuni et al. At $T = 4500$ K, however, the RT band becomes more important and the CIA spectrum is affected at all frequencies. Interestingly enough, we note that since the opacity is changed at all frequencies by comparable amounts, the effects on the model atmosphere calculations are totally negligible, a result which has been verified numerically.

Previous model calculations of cool white dwarf atmospheres (see, e.g., Shipman 1977; Mould & Liebert 1978) employed the H_2-H_2 CIA coefficients of Linsky (1969). A comparison of the cross-section calculations of Linsky at $T = 3000$ K with those of Zheng & Borysow (1994) reveals that the peak value of the RT band is about 4 times larger in the latter calculations, although both peaks are located at approximately the same wavelength (~ 5 μm). At higher temperatures, however, the peak of the RT band in the Zheng & Borysow calculations is displaced toward shorter wavelengths with the absorption coefficient peaking at 4.2 and 3.8 μm for $T = 4500$ and 6000 K, respectively. This result is a consequence of the weak dependence of the induced dipoles on the rotational quantum numbers (j). This j-dependence is particularly important at high temperatures and is treated in detail in the calculations of Zheng & Borysow (1994).

As discussed by Lenzuni et al., the peak value of the $v = 0 \rightarrow 1$ RV band at $\lambda \sim 2.5$ μm is about 1.5 times larger in the calculations of Borysow & Frommhold (1990) at $T = 3000$ K than estimated by Patch (1971). We note that the calculations of Patch (1971) already predict a peak value a factor of 2 larger than that obtained by Linsky. In the blue wing of the overall absorption profile ($\lambda \lesssim 1.6$ μm), however, earlier calculations of the collision-induced opacity were strongly *overestimated* (see Lenzuni et al. for a more complete discussion). These last results are particularly relevant to the present study, since the energy distributions of cool white dwarfs peak in this wavelength range.

In helium-rich models, the absorption by molecular hydrogen due to collisions with *helium* may become an important source of opacity in the infrared. The results of Lenzuni et al. (1991) indicate that the peak absorption of the H_2-He collision-induced opacity at $T = 3000$ K produced by the RT transitions is about 30 times stronger than predicted by Linsky (1969), while the peak originating from the $\Delta v = 1$ RV transitions is about 5 times larger. Furthermore, Linsky did not consider the first and second overtone bands ($\Delta v = 2$ and 3), an omission which results in a strong underestimate of the monochromatic opacity for $\lambda \lesssim 1.3$ μm.

2.2. *The Equation of Radiative Equilibrium*

Since the preliminary results of Bergeron, Ruiz, & Leggett (1994; see also Ruiz, Bergeron, & Leggett 1993) present no evidence for white dwarfs (hydrogen- or helium-dominated atmospheres) cooler than $T_{\rm eff} = 4000$ K, we adopt this temperature as the lower limit of our model grid calculations. The temperature and pressure structures of our pure hydrogen models at $\log g = 8$ are displayed in Figure 2. Also indicated are the locations of the photosphere ($\tau_R \sim \frac{2}{3}$) and the regions where the convective flux amounts to 1% of the total flux near the top of the convection zone. As discussed in great detail by Saumon et al. (1994a), there is a range of effective temperatures where it is nearly impossible to obtain an acceptable solution with the standard technique of linearizing the equations of atmospheric structure. We further develop some of the arguments presented in that paper.

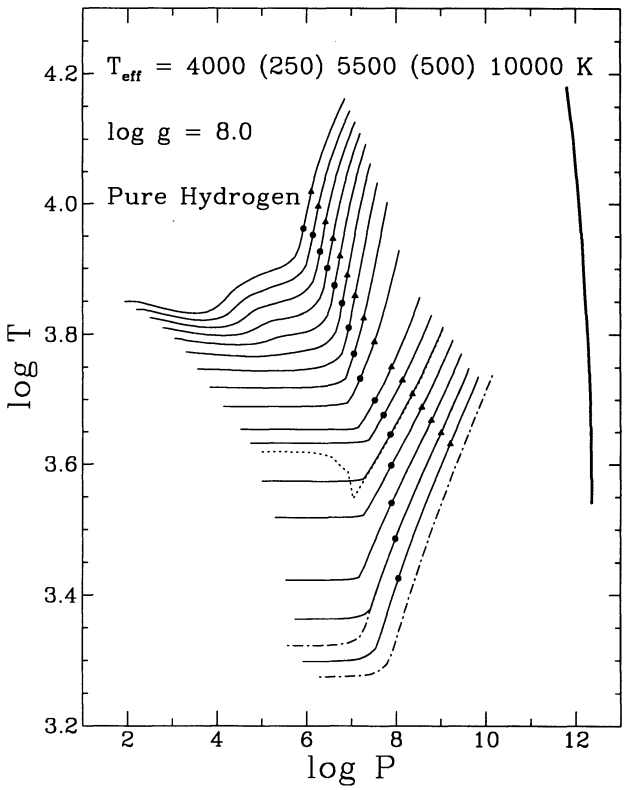

FIG. 2.—Temperature (in K) and pressure (in dyn cm^{-2}) stratifications of the pure hydrogen models at $\log g = 8$ (*solid lines*). Values of $T_{\rm eff}$ are indicated at the top; numbers in parentheses indicate the step in temperature. For each model, the location of the photosphere ($\tau_R \sim \frac{2}{3}$) is indicated by a triangle, and the regions where the convective flux transports 1% of the total flux near the top of the convection zone are marked by filled circles. Models at $T_{\rm eff} = 4000$ K, $\log g = 7.5$ and 8.5 are shown as dash-dotted lines, while the dotted line refers to the 5000 K pathological model discussed in the text (§ 2.2). The top and bottom layers of each model atmosphere are located at approximately $\tau_R \sim 10^{-6}$ and 100, respectively. The thick line represents the plasma phase transition predicted by Saumon & Chabrier (1992).

In the radiative superficial layers of cool model atmospheres, the temperature correction is governed mainly by the constraint of radiative equilibrium,

$$\int_0^\infty \kappa_\nu(T, P)[J_\nu(T, P) - B_\nu(T)]\, d\nu = 0\,. \qquad (1)$$

Figure 3 illustrates the behavior, as a function of a local temperature variation, of this integral at various depth points in a $T_{\rm eff} = 5000$ K gray model. The local temperature is thus varied at a given layer while keeping all other physical quantities constant. The behavior of the integral shown here is unique, to our knowledge, and reflects the nature of the opacity sources at play. In this particular regime of pressure and temperature, an *increase* in temperature produces more free electrons which enhance the H^- opacity, while a *decrease* in temperature favors the recombination of molecular hydrogen and thus increases the collision-induced opacity by H_2. There is therefore a regime of temperatures (associated roughly with the regime of molecular dissociation of H_2) where the opacity reaches a local *minimum*. The competition between these two absorption mechanisms is responsible for the variations observed in Figure 3 and, in particular, for the existence of local minima and maxima.

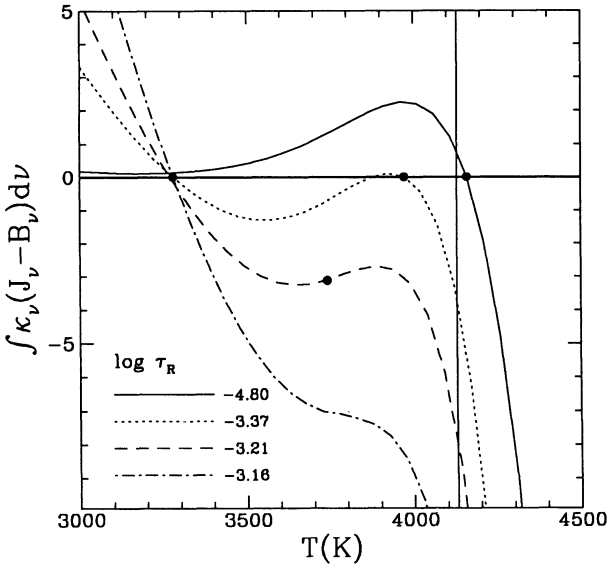

FIG. 3.—Value of the radiative equilibrium integral (in units of 10^6 ergs s^{-1} g^{-1}) calculated at several depth points in a nongray model at $T_{\rm eff} = 5000$ K and $\log g = 8.0$. The optical depth of each individual layer is indicated in the figure. Each curve illustrates the variations of the radiative equilibrium condition when only the *local* temperature is varied, while keeping all other physical quantities constant. The vertical line indicates the value of the temperature of the gray model used as the initial condition for the nongray correction procedure. The filled circles correspond to the temperatures of the nongray model converged with a standard linearization technique.

The solutions which satisfy the condition of radiative equilibrium correspond in Figure 3 to the roots on each curve. One can readily see that for some layers, more than one solution exists (this result is also nicely illustrated in Saumon et al. 1994a, Fig. 2). Since the correction in temperature is obtained from a linearized version of equation (1), which is basically a Newton-Raphson method, one can easily follow in Figure 3 the iterative sequence of temperature corrections starting from the gray temperature of the initial model (indicated by a vertical line). In the uppermost layer displayed here, the temperature will increase to approach the radiative-equilibrium solution while it will tend to decrease in the deeper layers. At $\log \tau_R = -3.37$, the iterations will stop when the first root located at $T = 3970$ K is encountered, while at $\log \tau_R = -3.21$, the procedure will stop after going over the bump around 3900 K where there is a local maximum in the function (i.e., where the integral in eq. [1] approaches zero the most). At $\log \tau_R = -3.16$, the correction procedure will drive the temperature to the only existing root at $T \sim 3300$ K since there are no local minima or maxima at that depth. The overall result of this correction procedure is to create a strong discontinuity in temperature in the *converged* model. Such a model at $T_{\rm eff} = 5000$ K is displayed in Figure 2 (*dotted line*); other examples are shown in Saumon et al. (1994a, Fig. 2). At $\log g = 8.0$, strong dips appear only in models comprised between 4750 and 5250 K, with a weak variation of this range of $T_{\rm eff}$ with $\log g$ and $N({\rm He})/N({\rm H})$.

This problem can be solved, at least in some layers, by adjusting manually the initial conditions in temperature to incite the correction procedure toward the "correct" root (e.g., by starting at $T \lesssim 3500$ K in Fig. 3). However, the uppermost layer in Figure 3, and all layers above this depth point, show only one root at $T \sim 4150$ K. Around $T \sim 3300$ K, where all deeper layers converge, there is a local minimum where the radiative equilibrium condition only *approaches* zero. Even though this solution would still be acceptable,[4] the slope of the function at this point is close to zero, and the temperature corrections are correspondingly extremely large. These large corrections in T will eventually move the temperature back to the hot solution. Therefore, a high temperature plateau unavoidably develops in these models when a linearized version of equation (1) is used to drive the temperature corrections.

The solution to this problem, as discussed at length by Saumon et al. (1994a), is to derive a temperature correction from the difference between the integrated radiative Eddington fluxes at T and $T + \delta T$. The main drawback of this approach is the extremely slow convergence properties, in addition to the iterative procedure itself, which eventually stops when the local radiative flux is entirely decoupled from the local temperature. Since we are interested only in the regions where the continuum flux is formed, these problems are of no consequence. Experiments with both versions of the correction procedure in models where the temperature discontinuity does not occur indicate that the temperature and pressure structures are identical deeper than $\tau_R \sim 10^{-2}$, although small differences are found in the upper layers. These differences are responsible for the irregular variations in surface temperature (as a function of $T_{\rm eff}$) observed in Figure 2 for models in the range 4750–5250 K, for which the modified correction procedure was employed.

2.3. *Selected Results*

The results of Figure 2 indicate that the convection zone reaches smaller optical depths with decreasing effective temperature. This effect can be explained in terms of the enhanced cooling of the upper layers due to the presence of collision-induced absorption processes (see below). In the hotter models ($T_{\rm eff} \gtrsim 7500$ K), the effect of hydrogen line blanketing on the atmospheric structure is also observed. Models at $T_{\rm eff} = 4000$ K and $\log g = 7.5$ and 8.5 are displayed in Figure 2 as well.

With these tools in hand, it is now straightforward to calculate realistic white dwarf models with mixed helium and hydrogen compositions, a task never accomplished before at these low temperatures ($T_{\rm eff} \lesssim 6000$ K). The effect of the CIA on the temperature structure of the model atmospheres is illustrated in Figure 4. For the pure hydrogen composition, temperature profiles are displayed for both a gray and nongray model atmospheres. A more detailed study of these two models reveals that the surface cooling is caused by the presence of the CIA processes in the upper layers. In pure hydrogen models, the H_2-H_2 collision-induced opacity reduces the surface temperature by $\sim$25%. The effect is even more dramatic in helium-rich models where the contribution of the H_2-He CIA reduces the surface temperature even further. In the model with $N({\rm He})/N({\rm H}) = 10$, the surface temperature is reduced by more than 40% with respect to the nongray, pure hydrogen model, while the temperature in the deepest layers ($\tau_R = 10^2$) is increased by $\sim$15%. These results are a direct consequence of the nongray behavior of the collision-induced absorption profiles. At higher temperatures ($T_{\rm eff} \gtrsim 5000$ K), on the other hand, the opacity is dominated by the bound-free and free-free absorptions by H^-. Since this opacity is only weakly frequency

[4] With such a solution, total flux conservation is about 0.01%, while eq. (1) is satisfied to better than 0.03% when normalized to the total flux value.

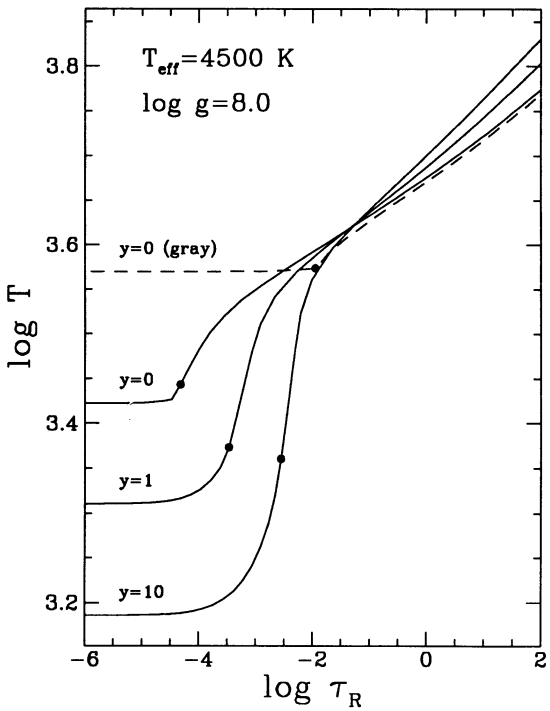

FIG. 4.—Temperature stratifications of models at $T_{\rm eff} = 4500$ K, log $g = 8.0$ and chemical compositions as indicated in the figure [$y = N$(He)/N(H)]. The dashed curve represents a gray model stratification. On each curve, the filled circle indicates the location of the first convective layer.

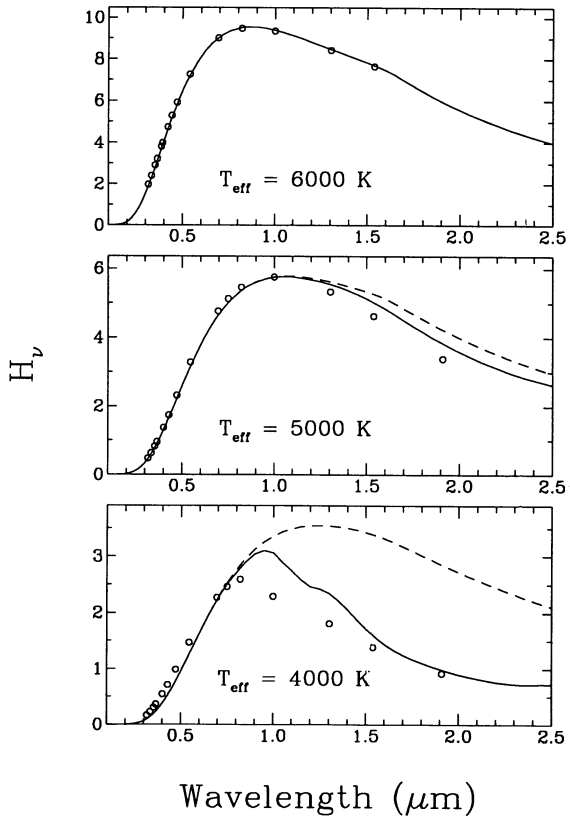

FIG. 5.—Energy distributions (Eddington fluxes in units of 10^{-6} ergs cm^{-2} s^{-1} Hz^{-1} sr^{-1}) of models at log $g = 8.0$ and pure hydrogen compositions. The solid curves represent our calculations including the collision-induced absorptions by H_2, while the dashed curves represent the fluxes calculated from the same atmospheric structures, but with all CIA opacities turned off. The open circles indicate the monochromatic fluxes taken from the models of Shipman (1977) calculated with the CIA coefficients of Linsky (1969).

dependent, the gray and nongray models (not shown here) are practically identical.

As discussed above, the cooling of the upper layers is governed by the requirement of radiative equilibrium in these layers in which the collision-induced opacity is the dominant absorption process. Such cooling affects the location of the top of the convection zone which rises in the atmosphere with respect to the gray model, as indicated in Figure 4. Interestingly enough, the locations of the first convective layer in each model do not correspond necessarily to the regions where the surface temperature becomes uniform.

In Figure 5, we compare our predicted energy distributions for pure hydrogen compositions with those of Shipman (1977). To illustrate the importance of the CIA on the emergent flux, we also display the energy distributions calculated from the same atmospheric structures, but with all collision-induced opacities turned off; the integrated flux is thus not equal to $\sigma T_{\rm eff}^4/4\pi$ in these calculations, and they only serve as a comparison. We also point out that the CIA process in pure hydrogen models is completely dominated by the H_2-H_2 interaction, since the contribution of the H_2-H interaction becomes important only in a regime where the abundance of neutral hydrogen is significant, in which case the total opacity is dominated by the bound-free and free-free absorptions by H^-. At $T_{\rm eff} = 6000$ K, the agreement between our predicted fluxes and those of Shipman is excellent, a consequence of the fact that the contribution of the CIA to the total opacity is negligible at that temperature. In cooler models, however, the CIA becomes increasingly important and eventually dominates the energy distribution in the infrared at $T_{\rm eff} = 4000$ K. It is also in the cooler models that significant departures from Shipman's models can be observed, a result which reflects the difference between the CIA opacities of Linsky (1969) used in his calculations and the CIA formalism described above. As discussed previously, the region of maximum flux of these cool white dwarf models ($\lambda \sim 1$ μm) corresponds to the frequency domain where the collision-induced opacity used in our calculations is *smaller* than that of Linsky. This results in an increased emergent flux in the 0.8–1.5 μm range at 4000 K with respect to the fluxes calculated by Shipman.

Figure 6 shows the energy distributions of model atmospheres with $T_{\rm eff} = 4500$ K, log $g = 8.0$, and various chemical compositions. These results indicate that the emergent fluxes of cool white dwarfs, and especially those with a helium-rich composition, differ significantly from the energy distribution of a blackbody at the same temperature. In the helium-rich models, the absorption by molecular hydrogen due to collisions with helium becomes a dominant source of opacity in the infrared. Even white dwarfs with N(He)/N(H) ~ 1 would have energy distributions that are markedly different from those of pure hydrogen atmospheres. Such cool, helium-rich white dwarfs can easily be recognized in two-color diagrams (see § 4). Recently, Bergeron et al. (1994b) have successfully explained the strong infrared flux deficiency observed in the peculiar cool white dwarf LHS 1126 in terms of H_2-He collision-induced absorptions. This process had never been included in previous calculations of white dwarf model atmospheres.

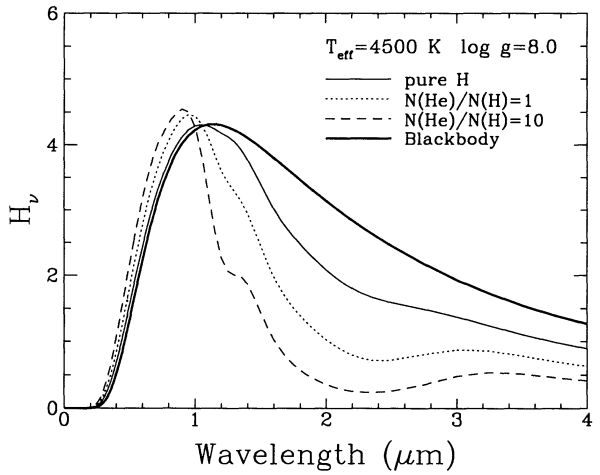

FIG. 6.—Energy distributions (Eddington fluxes in units of 10^{-6} ergs cm^{-2} s^{-1} Hz^{-1} sr^{-1}) of models at $T_{\rm eff}$ = 4500 K, log g = 8.0 and various chemical compositions. Those are compared with a blackbody energy distribution at the same temperature.

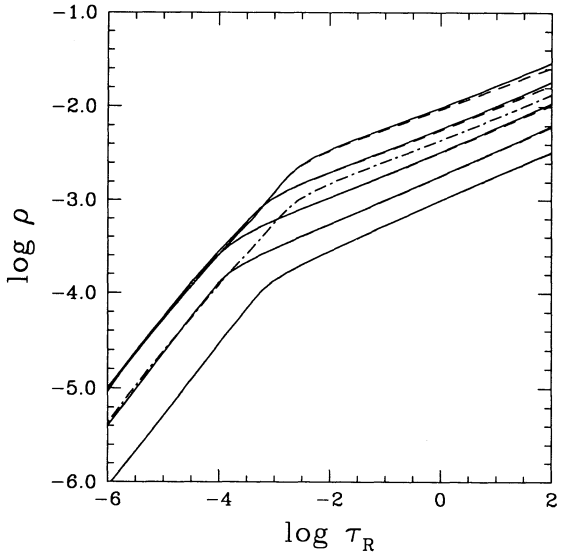

FIG. 7.—Density (in g cm^{-3}) profiles for pure hydrogen models at log g = 8.0 and temperatures of (from top to bottom) 4000, 4250, 4500, 4750, and 5000 K. Densities have been calculated from the (T, P) structures obtained in this study assuming an ideal gas (*solid lines*), and they are compared with the densities obtained from the EOS of Saumon & Chabrier (1992; *dashed lines*). The dash-dotted line indicates a model at $T_{\rm eff}$ = 4000 K and log g = 7.5 (ideal gas).

2.4. *Nonideal Effects in the Hydrogen Equation of State*

EOSs provide the basic thermodynamic quantities needed to determine the physical properties of stellar and planetary *interiors*. However, they usually do not provide detailed atomic or molecular populations that are generally required to obtain the monochromatic opacity, a quantity which is crucial to the calculations of realistic stellar *atmospheres*. Therefore, the calculations of model atmospheres which take into account nonideal effects in the EOS can only be performed approximately by combining EOS computations with radiative opacities calculated independently with different physical assumptions. Here, we simply compare the densities obtained from the models calculated above (ideal gas) with those computed from the EOS of Saumon & Chabrier (1992) in which nonideal effects are carefully accounted for.

Figure 7 shows the comparison of density profiles in the coolest models ($T_{\rm eff} \leq$ 5000 K, log g = 8.0) of our pure hydrogen grid. The observed differences are always relatively small in the regions where the continuum flux is formed. At $\tau_R \sim \frac{2}{3}$, the relative differences are 4.8%, 1.4%, and 0.4% for models with $T_{\rm eff}$ = 4000, 4500, and 5000 K, respectively. In the deeper layers (τ_R = 100), however, densities differ by $\sim$15% at $T_{\rm eff}$ = 4000 K, but these differences rapidly drop to 10% and only 2% at $T_{\rm eff}$ = 4500 and 5000 K, respectively. In contrast, a small change in surface gravity produces changes in the density profiles that are much more important, as illustrated in Figure 7 where the density profile of a $T_{\rm eff}$ = 4000 K, log g = 7.5 pure hydrogen model is displayed. We thus conclude that nonideal effects are negligible for the calculations of cool, pure hydrogen atmospheres and that the use of an ideal gas approximation is justified.

As discussed below (§ 3.2), nonideal effects become important for cool, pure helium models. This result is a consequence of the extremely high atmospheric pressures reached in the photospheric regions of these models, owing to the low opacity of pure helium under these conditions. Therefore, as long as there are sufficient amounts of hydrogen to ensure low atmospheric pressures, nonideal effects should be small. This is certainly the case with the mixed H/He models calculated here, and we conclude that nonideal effects are negligible in these models as well. We also point out that even the most extreme models of our grid are located in a region of the (T, P) plane comfortably away from the regime of pressure ionization of hydrogen and from the plasma phase transition predicted by Saumon & Chabrier (1992; see Fig. 2).

3. THE PURE HELIUM MODELS

3.1. *Previous Model Calculations*

Previous calculations of white dwarf atmospheres with helium-rich or pure helium compositions include those of Böhm et al. (1977), Mould & Liebert (1978), and Kapranidis (1983). In the Mould & Liebert calculations, which are based on a modified version of the ATLAS code, all models have temperatures above $T_{\rm eff}$ = 4000 K, where the effects of photospheric degeneracy are negligible according to the exploratory calculations of Böhm et al. (1977).

A major step forward has been taken by Kapranidis (1983), who incorporated an improved version of the EOS of Carson, Mayers, & Stibbs (1968) based on a hot Thomas-Fermi model of the helium gas. Kapranidis (1983) also included in a self-consistent manner the energy transport by electron thermal conduction (along with energy transport by radiation and convection) which was found to be important in models below $T_{\rm eff} \sim$ 4000 K, when pressure ionization and electron degeneracy prevail. This result had already been anticipated in the earlier calculations of Böhm et al. (1977), although energy transport by conduction had not been treated in detail in their analysis. Even though the much more detailed and improved EOS calculations of Fontaine, Graboske, & Van Horn (1977; hereafter FGVH) were available at that time, the results of Carson had the advantage of including radiative and conductive opacities calculated self-consistently with the assumed EOS. As discussed by Kapranidis (1983), the combination of radiative and conductive opacities with independent EOS calculations can lead to several inconsistencies since the opacity in a cool helium plasma depends strongly on the degree of

ionization, which in turn may vary widely amongst various EOS calculations. For these reasons, Kapranidis preferred to rely on the EOS of Carson since the aim of his study was to determine the importance of conductive energy transport in cool degenerate atmospheres.

3.2. *Nonideal Effects in the Helium Equation of State*

In this section, we study the sensitivity of the atmospheric structure of pure helium models to nonideal effects in the EOS. In particular, we compare models calculated with an ideal gas EOS with those obtained from the EOS of FGVH, and also from a modified version (see § 3.2.2 below) of the EOS of Saumon, Chabrier & Van Horn (1994b; hereafter SCVH).

We first restrict our comparison to the EOS properties only [i.e., the effects of varying the $\rho(P, T)$ relation, adiabatic gradient, specific heat, etc.] and put aside—for the time being—the complications associated with the calculation of the degree of ionization. For this purpose, we assume that the ionization equilibrium is given by the Saha equations throughout. This approximation is clearly not valid at high densities and low temperatures, but it is adequate for this comparison. In other words, we assume an electron density relation $N_e(P, T)$ based on the Saha ionization equilibrium and which is independent of the details of the EOS. The ionization equilibrium will be studied in greater detail in § 3.3. In the following, we consider only gray stratifications and neglect the energy transport by conduction.

We first consider the EOS calculated by FGVH for a pure helium composition (the so-called Iben V mixture). Here we use a modified version of these calculations generously provided to us by G. Fontaine, in which small numerical errors found in the earlier calculations have been corrected. Since the FGVH tabulations extend only up to $\log \rho = \frac{1}{3}$ ($\log P \sim 12.6$) extrapolations outside the tables were used to calculate the coolest models ($T_{\rm eff} \lesssim 5500$ K). Even though the extrapolations were smooth, these models should be regarded with caution.

The results of our calculations are displayed in Figure 8. Surprisingly, the comparison shows that the temperature and pressure structures of models calculated from an ideal gas are hardly affected by the use of the EOS of FGVH, in which nonideal effects are taken into account. These results do not necessarily imply that nonideal effects are negligible, however. Indeed, the density profiles shown in Figure 8 are markedly different, with the densities from the FGVH models being significantly smaller than those obtained from the ideal gas approximation. These differences are especially noticeable at low temperatures and high atmospheric pressures where nonideal effects in the EOS are predominant. The small observed effects on the T-P structures can be understood qualitatively in terms of the three basic equations which govern the atmospheric structure. The equation of hydrostatic equilibrium ($dP/d\tau_{\rm R} = g/\kappa_{\rm R}$) depends mainly on the opacity which, in turn, depends strictly on the value of the electron density in such cool pure helium atmospheres (see § 3.3). But as mentioned above, the $N_e(P, T)$ relations are assumed identical for all model calculations. The same reasoning applies to the equation of radiative transfer and also to the constraint of radiative equilibrium in the upper layers. In the deeper layers, however, the temperature and pressure stratifications are governed by the energy transport by convection. In these cool atmospheres where convection is strongly adiabatic, the atmospheric structures are completely described by the adiabatic gradient whose value is very sensitive to the various nonideal effects included in the EOS. For instance, in the FGVH model at $T_{\rm eff} = 5500$ K (see Fig. 8), the adiabatic gradient drops from a value of $\nabla_{\rm ad} = 0.4$ at the surface to a minimum value of ~ 0.25 at $\tau_{\rm R} \sim 10^{-4}$ and increases back up to $\nabla_{\rm ad} \sim 0.33$ in the convection zone, while in the ideal gas model, $\nabla_{\rm ad} = 0.4$ throughout. The small differences in the T and P structures displayed in Figure 8 can be fully accounted for by these differences in $\nabla_{\rm ad}$.

A further comparison can be made with the EOS calculations of SCVH as shown by the dashed lines on Figure 8. Perhaps not surprisingly this time, the EOS of SCVH does not affect the temperature and pressure stratifications substantially. The density profiles are quite different, as expected, with the densities of the SCVH models having intermediate values between the FGVH models and those calculated from the ideal gas approximation. We thus conclude that in the range of effective temperatures considered in this analysis, *and for a given $N_e(P, T)$ relation*, nonideal effects in the EOS have negligible effects on the P and T stratifications, although mass densities are strongly affected by the particular choice of the EOS. On the other hand, in a self-consistent calculation, the opacity depends on the density and on the degree of ionization, which is mainly dictated by the nonideal effects. Similarly, the adiabatic gradient is found to be sensitive on the nature of the nonideal terms in the EOS. We therefore adopt the (modified) EOS of SCVH since it provides a realistic description of the interactions in a very weakly ionized He fluid, as discussed below.

3.3. *The Ionization Equilibrium*

At sufficiently low densities and low temperatures, the helium gas is practically neutral, and the very few free electrons do not affect the general thermodynamic properties of the gas. As a consequence, most EOS calculations do not usually treat the ionization equilibrium with a high degree of accuracy under such conditions (see the discussion by Hummer & Mihalas 1988). Because the cross section of He^- free-free absorption is very large, and because this absorption process plays a central role in cool, pure He atmospheres, it is very important to determine accurately the electron density, or equivalently, the degree of ionization, even when it is as small as $N_e/N_{\rm He} \approx 10^{-20}$. In this context, the free electrons are provided by temperature ionization and by very weak pressure ionization caused by the interactions between He atoms which overwhelmingly dominate the composition of the gas. In the following discussion, we apply the term "pressure ionization" to the relatively weak ionization caused by nonideal effects in the EOS. Usually, it refers to the often abrupt transition from a roughly nonionized fluid to a fully ionized, metallic state. This typically occurs at very high pressures of the order of 1–100 Mbar ($\log P = 12$–14) for hydrogen and helium.

3.3.1. *Results with the FGVH Equation of State*

FGVH mention that the dimensionless chemical potential of the electrons, $\eta = \mu_e/kT$, is a secondary parameter in their calculations and that no effort has been made to establish accurate values in the low-density regime. As such, values of η become unreliable for $\eta \lesssim -5$, where the electrons are essentially nondegenerate. To correct this situation, G. Fontaine has kindly calculated for us new values of η based on an improved version of the FGVH EOS. In particular, the ionization equilibrium and thus the value of η are now obtained from the Saha equation up to the point where nonideal effects become impor-

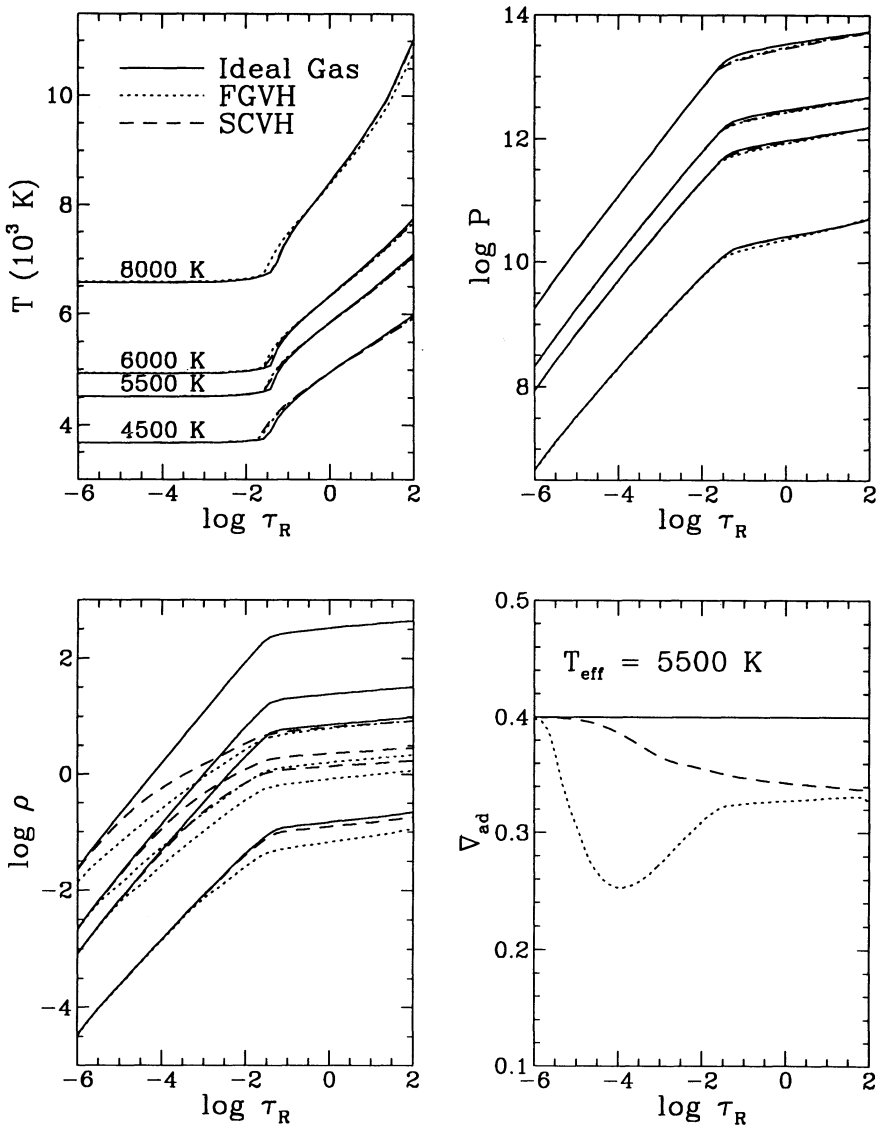

FIG. 8.—Comparison of the temperature, pressure (in dyn cm^{-3}), and density (in g cm^{-3}) profiles of pure helium models calculated under the assumption of an ideal gas (*solid lines*), the EOS of FGVH (*dotted lines*), and a modified version of the EOS of SCVH (see text; *dashed lines*). The adiabatic gradient is also shown for a $T_{\rm eff}$ = 5500 K model. All models have log g = 8.0, and temperatures are indicated on the plot. The Saha equation for the ionization equilibrium has been assumed throughout.

tant within the FGVH approximations (log $\rho \leq -13/3$ for log $T < 4.18$). Above this value of density, nonideal effects become important, and the FMIN method described by FGVH provides unreliable values for η until the electrons become degenerate, as discussed above. In the present calculations, this corresponds to mass densities larger than log $\rho = -\frac{2}{3}$. In the intermediate density regime where the value of η is unreliable ($-13/3 <$ log $\rho < -2/3$), we have used a smooth cubic spline interpolation to evaluate η. This procedure is illustrated in Figure 9. Under these approximations, it is then straightforward to calculate the electron density from the $F_{1/2}(\eta)$ Fermi-Dirac functions at all densities and temperatures. Throughout our calculations, we assume that neutral helium is in the ground state. At the pressures relevant to these atmospheres, this is an excellent approximation for log $T \leq 4.2$. When pressure ionization begins, we further assume that both electrons are removed at once so that $N_{\rm He\ III} = 0.5N_e$ and $N_{\rm He\ II} \equiv 0$. The latter approximation is not crucial since He II and He III never contribute to the opacity.

The variation of the electron density with total pressure is displayed in Figure 10 for an isotherm at T = 4500 K. Electron densities obtained from the Saha equation and those tabulated by Carson (1977; see also Kapranidis 1982) and used by Kapranidis (1983) are also shown for comparison (the curve labeled "this study" is described in § 3.3.2). On each curve, the departure of the electron density from the value obtained with the Saha approximation indicates the region where pressure ionization sets in. The curves then saturate when complete pressure ionization is reached. Since the degree of ionization is very low throughout the atmosphere, the free electrons and helium ions do not contribute significantly to the nonideal terms of the EOS and do not affect the internal structure of the atoms. This follows from the fact that the Debye screening length is very much larger than both the Bohr radius and the interparticle

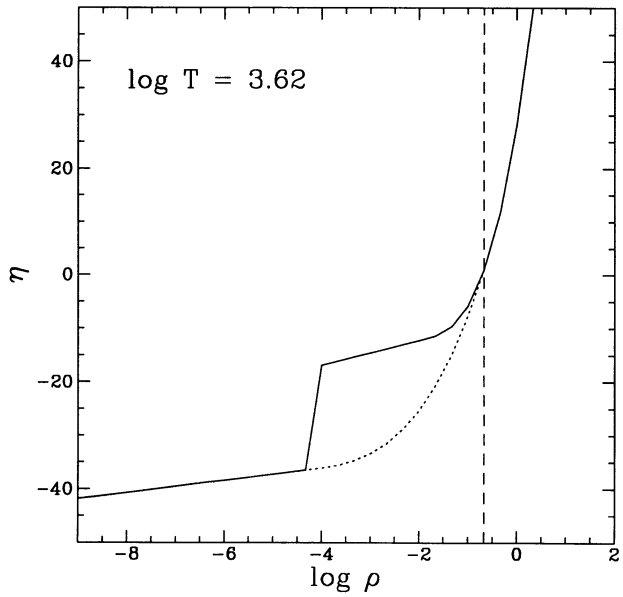

FIG. 9.—Value of the degeneracy parameter as a function of the mass density (in g cm^{-3}) taken from the modified tables of FGVH (see text) for an illustrative isotherm at log $T = 3.62$. The solid line indicates the value of η obtained directly from the tables, while the dotted line represents our smooth interpolation between the regime where the Saha equation is valid (log $\rho \leq -13/3$) and the regime where electron degeneracy becomes important, i.e., where η yields accurate value for N_e (log $\rho \geq -\frac{2}{3}$; *dashed line*).

distance. The nonideal effects arise almost entirely from the repulsive forces from neighboring helium atoms. These forces rise very rapidly at short distances and raise the energy of the atomic state with respect to that of ionized helium, thus favoring ionization. This is the origin of low-temperature pressure ionization.

Models at $T_{\rm eff} = 4500$ K and log $g = 8.0$ calculated with various ionization models are displayed in Figure 11. For the moment, we consider only the model labeled FGVH, which is a gray model obtained with the EOS of FGVH and the electron density derived from the value of η and that labeled "Saha," which is calculated under the assumptions of an ideal gas and the Saha equation for the ionization equilibrium. Even though ionization is small at the photosphere of the FGVH model ($N_e/N_{\rm He} \sim 6 \times 10^{-8}$), the corresponding electron density is still 10^6–10^7 times larger than that obtained from the Saha equation (refer to Fig. 10 with $T \sim 4500$ K and log $P \sim 10$ at the photosphere). Consequently, these free electrons increase by several orders of magnitude the contribution of the He^- free-free opacity to the total opacity, which otherwise would be dominated by the Rayleigh scattering by neutral helium. The direct consequence of this increase in opacity is a dramatic reduction of the atmospheric pressure, as observed in Figure 11, with respect to models calculated with the Saha equation. We showed earlier that nonideal effects in the EOS calculations do not have a significant *direct* effect on the structure of the models (see Fig. 8). However, they do have an important *indirect* influence by promoting pressure ionization which makes free electrons available for the dominant He^- absorption. From this perspective, the treatment of the nonideal effects in fluid atomic helium requires careful attention.

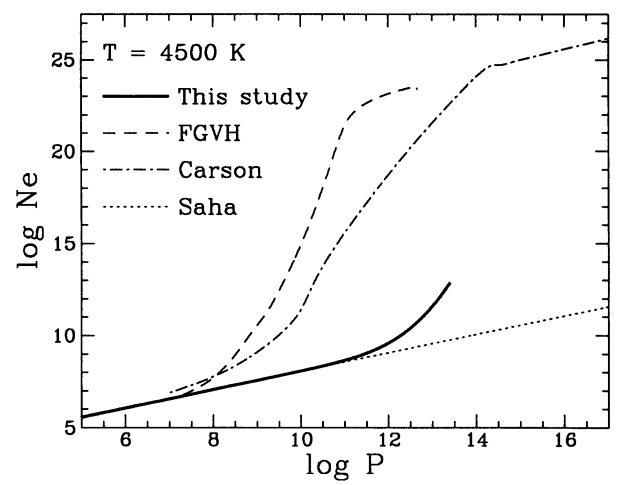

FIG. 10.—Electron number density (in cm^{-3}) in a pure helium plasma as a function of total pressure (in dyn cm^{-3}), calculated at $T = 4500$ K under various assumptions: (1) from the Saha equation for the ionization equilibrium (*dotted line*), (2) from the η parameter obtained from the EOS of FGVH (*dashed line*), (3) from the EOS of Carson (1977; *dash-dotted line*), and (4) from the pressure ionization model described in § 3.3.2 and used in this study (*thick solid line*).

3.3.2. *An Improved Treatment of Pressure Ionization*

In the EOS of FGVH, the strong, short-range repulsive forces between He atoms are represented by a hard sphere model. This "billiard ball" image of the atom is qualitatively correct in first approximation, but it fails to take into account the softness of the repulsive core of the He-He potential. Actual interatomic potentials are not infinitely repulsive like hard spheres, as demonstrated by ab initio quantum mechanical calculations and by high-pressure experiments. Saumon & Chabrier (1992) and SCVH have argued convincingly that the hard sphere potential is too harsh and overestimates the magnitude of the interatomic nonideal effects (here, the He-He repulsion). This is illustrated in figures of hydrogen EOS comparison in SCVH. It is revealing that departures between the EOS of SCVH and FGVH arise for log $P > 8$, roughly the same pressure where the degree of ionization of FGVH departs significantly from the Saha results (Fig. 10). This also suggests that the hard sphere diameter in FGVH (essentially a free parameter in the calculation) is too large. There are therefore good reasons to suspect that the degree of ionization in the FGVH EOS, shown in Figure 10, is overestimated.

The EOS of SCVH and the modified version used here are based on a He-He potential determined experimentally to pressures of up to log $P = 11.7$ (Nellis et al. 1984). There is no evidence in these experiments supporting the full pressure ionization obtained by FGVH at this pressure (Fig. 10). The detailed calculation of the nonideal effects can be found in SCVH. In these original calculations, however, the ionization equilibrium was not determined accurately in the limit of low temperatures and low densities, where the helium gas was considered neutral. Therefore it is not possible to obtain reliable electron densities from these calculations.

For the present purpose, the helium EOS was recomputed to allow ionization of He with an entirely different numerical method to obtain an accurate chemical equilibrium between He, He^+, and e. This calculation is limited to log $T < 4.2$, and thermal excitation of the atoms was neglected. At very low pressures, where nonideal effects are negligible, it recovers the limit provided by the Saha equations.

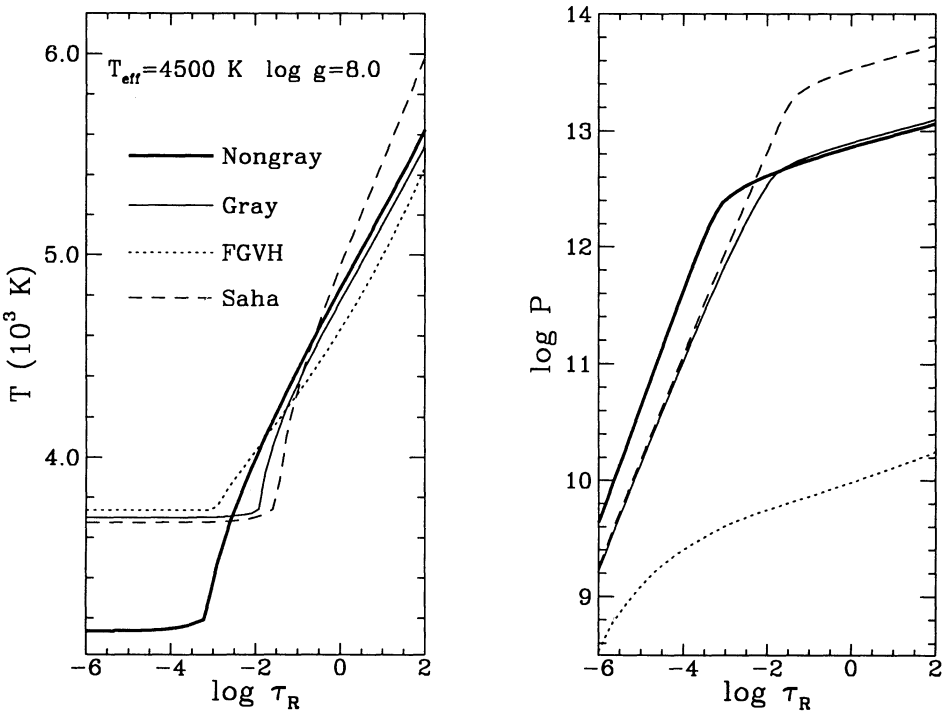

FIG. 11.—Temperature and pressure (in dyn cm^{-3}) stratifications for pure helium models with T_{eff} = 4500 K and log g = 8.0. All models are gray except that indicated by the thick solid line. Models have been calculated either with the EOS of FGVH and the electron density obtained from the corresponding value of η (*dotted line*), with an ideal gas EOS and the Saha equation for the ionization equilibrium (*thin dashed line*), or with the modified EOS of Saumon et al. (1994b; see text) and the pressure ionization model developed in this study (§ 3.3.2; *thin and thick solid lines*).

Because of the very high pressures obtained in these atmospheres, we must consider the possibility of reaching full pressure ionization. Pressure ionization is an exceedingly complex problem for any substance, and the case of helium remains largely unexplored, as discussed in SCVH. Various estimates indicate that it should occur between 10 and 50 g cm^{-3} and is probably close to 30 g cm^{-3}. The coolest helium atmospheres presented herein approach the lower limit of this range. One of the main difficulties lies in treating the Coulomb interaction between charged particles. When the degree of ionization is very low, the plasma is extremely dilute, and Coulomb terms are entirely negligible compared to the He-He interactions. When ionization is substantial, Coulomb interactions can become very large, an additional nonideal effect which favors further ionization since the Coulomb interactions lower the energy of the plasma compared to the atomic state. It follows that the density or pressure where full pressure ionization is obtained depends critically on the model for Coulomb interactions as well as for the interaction between charged and neutral particles. There is currently no satisfactory approach to this problem.

A good treatment of pressure ionization of helium is well outside the scope of this project, and we have favored the virtues of simplicity and consistency in our model for the EOS. By neglecting the Coulomb interactions altogether, the degree of ionization remains low enough to (1) be consistent with the approximation and (2) avoid complete pressure ionization. This is very reasonable since the highest densities reached by these model atmospheres ($\approx$5 g cm^{-3}) remain below the estimated range for complete pressure ionization of helium. In addition, complete pressure ionization would occur at such large optical depths in the atmosphere that it would not affect the emergent flux. In other words, it is unlikely that further improvement in our understanding of pressure ionization of helium will affect the outcome of this calculation significantly.

The heavy solid line of Figure 10 shows the electron density obtained with this model. There is a striking contrast between this calculation and the results of FGVH and of Carson (1977). The realistic He-He potential used here leads to a much weaker interaction at low pressures, and deviations from the Saha ionization equilibrium do not appear until much higher pressures. As we had anticipated, the hard sphere model of FGVH predicts a significantly higher degree of ionization. As we will see below, this difference in degree of ionization and the concomitant change in the He^- opacity are reflected in the emergent spectra of cool, pure helium white dwarf atmospheres.

Model atmospheres calculated with the pressure ionization model described above are displayed in Figure 11 for both gray and nongray structures. Since the electron densities calculated with the present EOS model are intermediate between those derived from the Saha equation and those obtained from the FGVH approximation (Fig. 10), the atmospheric pressures have consequently intermediate values as well. The onset of pressure ionization being at much larger values of P, the pressure stratifications of these models resemble more closely that obtained from the Saha equation. The temperature stratifications, however, vary considerably between the various calculations displayed in Figure 11. These results reinforce our conclusion that pressure ionization governs the atmospheric structure of pure helium models and that it is the largest source of disagreement between model atmosphere calculations.

The results of Figure 11 also indicate that nongray effects are important, with the surface temperature dropping by $\sim$600 K. In the deeper layers, however, the temperature increases by

only ~70 K. The surface cooling is due to the Rayleigh scattering opacity which dominates the total opacity in the upper layers where the atmospheric pressures are low. The Rayleigh scattering opacity is highly nongray, and the constraint of radiative equilibrium forces the surface temperature to decrease. Consequently, the top of the convection zone rises, and the temperature of the deeper regions slightly increases. Kapranidis (1983) calculated gray stratifications only, since the main purpose of his investigation was to determine qualitatively the influence of nonideal effects in the EOS, electron degeneracy, and electron thermal conduction, with a smaller emphasis on the predicted emergent fluxes. Kapranidis also argues that if nongray effects exist, they should not affect significantly the temperature structure of the deeper layers, in agreement with our results. However, even small departures such as those observed in Figure 11 yield important differences of about 10% in the emergent fluxes at 4000 Å and 3% at 2 μm. Therefore, nongray effects should not be neglected.

3.4. *Selected Results*

The temperature and pressure structures of our pure helium models at log $g = 8$ are displayed in Figure 12. As in Figure 2, we indicate the locations of the photosphere ($\tau_R \sim \frac{2}{3}$) and the regions where the convective flux transports 1% of the total flux near the top of the convection zone. Models at $T_{\rm eff} = 4000$ K and log $g = 7.5$ and 8.5 are also shown.

Some interesting properties of our atmosphere calculations are illustrated at the top of Figure 13, where we show the predicted emergent fluxes for models with $T_{\rm eff} = 5000$ K and various values of log g. The results indicate that the energy distributions vary considerably with log g, a direct consequence of our model of pressure ionization. At the bottom of Figure 13, we show the variation with log g of the monochromatic opacity at the photosphere ($\tau_R \sim \frac{2}{3}$) for the individual contributions of He^- free-free absorption and Rayleigh scattering by neutral helium; since the opacity is calculated per gram of matter, the Rayleigh scattering contribution is the same for all models. As pressure ionization increases in models with higher log g values, the electron density and the He^- free-free opacity increase correspondingly. The competition between the two opacity processes is responsible for the variations in the emergent fluxes with log g. The details of this sensitivity, however, depend on the value of the density where pressure ionization sets in. In the FGVH models, for instance, pressure ionization occurs at such low densities that the opacity is always dominated by He^- free-free absorptions. Consequently, the sensitivity to log g disappears, and the energy distributions all look identical at a given $T_{\rm eff}$. These energy distributions are comparable to those calculated here for the highest values of log g.

We also note that the energy distributions of pure helium models are significantly different from a blackbody energy distribution (Fig. 13), with the exception of models at high surface gravities in which He^- free-free is the dominant source of opacity. Since the latter is weakly frequency dependent, the atmosphere is relatively gray, and the corresponding emergent fluxes resemble more those of a blackbody. We finally remark

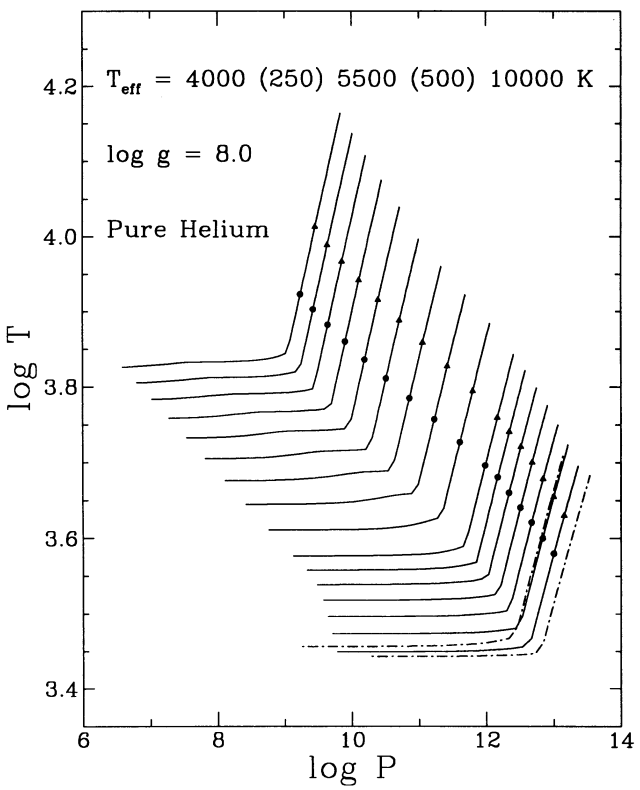

FIG. 12.—Same as Fig. 2 but for pure helium models

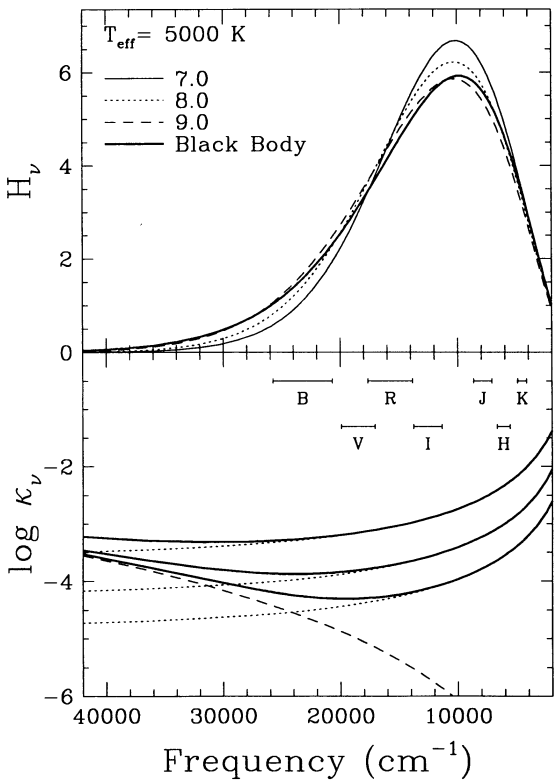

FIG. 13.—(*Top*) Energy distributions (Eddington fluxes in units of 10^{-6} ergs cm^{-2} s^{-1} Hz^{-1} sr^{-1}) of models at $T_{\rm eff} = 5000$ K with pure helium compositions and various values of log g. The thick line represents the energy distribution of a blackbody at the same temperature. (*Bottom*) Variation of the total monochromatic opacity (in cm^2 g^{-1}; *solid lines*) at the photosphere ($\tau_R \sim \frac{2}{3}$) of the models displayed at the top of the figure; log $g = 7.0$ has the lowest opacity. Also shown are the individual contributions from Rayleigh scattering by neutral helium (*dashed line*) and from the He^- free-free opacity (*dotted lines*). Note that since the opacity is *per gram*, the contribution from the Rayleigh scattering is identical for all models. The photometric bandpasses (FWHM) of the optical *BVRI* and infrared *JHK* filters are indicated in the bottom panel.

that the energy distributions of high-gravity objects can be reproduced to some extent if additional free electrons are provided by heavier elements present in the photospheric regions.

In Figure 14, we compare the observed energy distribution (optical *BVRI* and infrared *JHK* photometry) of a DC white dwarf, LP 754−16, with our best fits obtained from the models developed with the FGVH and the modified SCVH EOS. The data have been gathered as part of the ongoing photometric and spectroscopic survey of Ruiz et al. (1993); the data acquisition and reduction, as well as the fitting procedure, are similar to those outlined in Bergeron, Ruiz, & Leggett (1992). LP 754−16 is a typical object from the sample of Bergeron et al. (1994a), whose energy distribution can only be reproduced with a pure helium model. While the fit derived from our new models is excellent, that obtained from the FGVH models fails to match the observed fluxes at *B*, *I*, and *K*. This indicates that real white dwarf stars are better reproduced with models in which both He^- free-free absorptions *and* Rayleigh scattering by neutral helium contribute to the total opacity. There are several such objects with similar temperatures in the sample of Bergeron et al. (1994a), but the shape of the energy distributions varies considerably from object to object, a result which can readily be interpreted quantitatively in terms of a spread in log *g*. Such variations with log *g* cannot be achieved with the FGVH models for reasons outlined above. In particular, a different value of log *g* would not change the quality of our fit to LP 754−16 with the FGVH models. These results strongly suggest that pressure ionization does occur at much higher densities than those inferred in the calculations FGVH or Carson. The ability of our models to reproduce the observed energy distributions by varying the value of log *g* further reinforces our confidence in our pressure ionization model.

The main source of uncertainty in the input physics of our model atmosphere calculations is the free-free absorption cross-section of He^- at very high densities. We have used the standard low-density value. However, high pressures are reached only deep in the atmosphere, where convection dominates and the structure is very nearly adiabatic. Under these conditions, the atmospheric structure is fairly insensitive to the opacity.

Finally, we note that since pressure ionization proceeds at fairly high densities in our models, the density of free electrons is always small. Therefore, electron degeneracy is never important in the range of atmospheric parameters considered here, and energy transport by thermal electron conduction can be safely neglected. For example, in the deepest layers of our coolest model at $T_{\rm eff} = 4000$ K and log $g = 8.0$, the ionization fraction is still very small, $N_e/N_{\rm He} \sim 10^{-12}$, and the degeneracy parameter reaches values of only $\epsilon_F/kT < 10^{-5}$, where ϵ_F is the Fermi energy of the electrons. Since there is no evidence for stars cooler than $T_{\rm eff} = 4000$ K in the survey of Bergeron et al. (1994a), we conclude that electron conduction is unimportant in the atmospheres of cool, observable helium-rich white dwarfs.

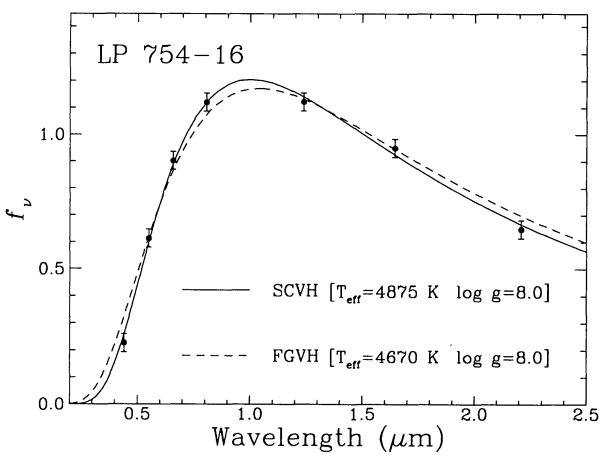

FIG. 14.—Our best fits to the energy distribution of the DC star LP 754−16 obtained from the ongoing survey of Ruiz et al. (1993). Fluxes are in units of 10^{-26} ergs cm^{-2} s^{-1} Hz^{-1}. All models have pure helium compositions; fits are presented for both the FGVH models and for those developed with our model of pressure ionization (see § 3.3.2).

4. BROADBAND COLOR CALCULATIONS

We have calculated broadband color indices for the complete grid of model atmospheres using the optical *BVRI* and infrared *JHK* passbands of Bessel (1990) and Bessel & Brett (1988), respectively. We have experimented with various absolute calibrations—those from the references above and some derived from published and unpublished models by Kurucz—and found systematic shifts in some two-color diagrams, most notably in the $(V-I, B-V)$ diagram, between the observed photometry of Bergeron et al. (1994a) and the predicted color indices. These discrepancies were successfully removed if the absolute calibration of the photometry was instead tied in with the *observed* fluxes of Vega as measured by Hayes (1985) and Mountain et al. (1985). This calibration was thus preferred and used in the following.

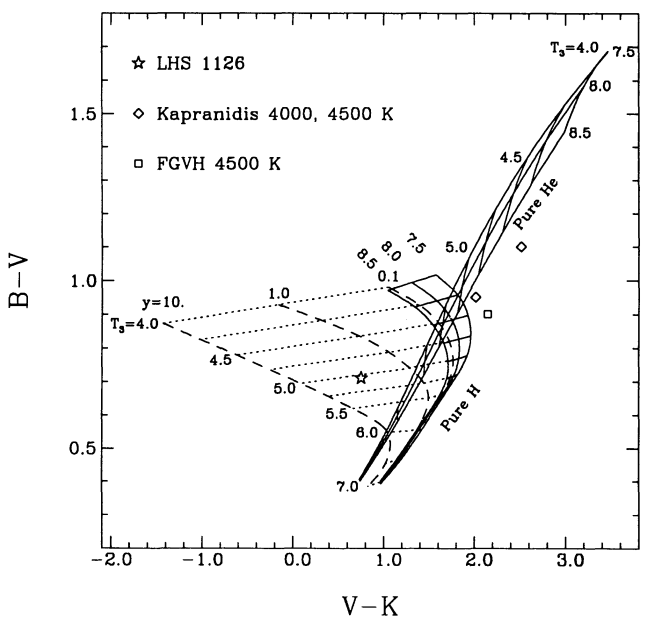

FIG. 15.—$(B-V, V-K)$ two-color diagram for various models from our complete grid. Pure hydrogen and pure helium models are indicated by solid lines for log $g = 7.5$, 8.0, 8.5 and temperatures in the range 4000–7000 K; models with the same value of log *g* or $T_{\rm eff}$ are connected by segments, and the corresponding values are indicated on the figure ($T_3 = T_{\rm eff}/10^3$ K). The dashed and dotted lines represent the log $g = 8.0$ models for various values of $y \equiv N({\rm He})/N({\rm H})$ and the same range of $T_{\rm eff}$. The star symbol indicates the location of LHS 1126 discussed in the text. Open diamonds indicate the location of the $T_{\rm eff} = 4000$ and 4500 K (log $g = 8.0$) pure helium models of Kapranidis (1985), while the open square corresponds to the FGVH pure helium model at $T_{\rm eff} = 4500$ K (log $g = 8.0$).

TABLE 1

BROADBAND COLOR INDICES OF THE PURE HYDROGEN MODELS

$T_{\rm eff}$ (K)	log g	$B-V$	$V-R$	$V-K$	$R-I$	$J-H$	$H-K$	BC(V)
4000.....	7.5	+1.02	+0.64	+1.58	+0.64	−0.08	−0.08	−0.35
4250.....	7.5	+0.96	+0.61	+1.81	+0.61	+0.03	−0.02	−0.37
4500.....	7.5	+0.90	+0.57	+1.93	+0.57	+0.15	+0.01	−0.36
4750.....	7.5	+0.84	+0.53	+1.96	+0.54	+0.24	+0.05	−0.33
5000.....	7.5	+0.78	+0.49	+1.92	+0.50	+0.28	+0.09	−0.29
5250.....	7.5	+0.72	+0.46	+1.81	+0.46	+0.28	+0.10	−0.25
5500.....	7.5	+0.66	+0.42	+1.67	+0.43	+0.27	+0.09	−0.21
6000.....	7.5	+0.55	+0.35	+1.41	+0.36	+0.25	+0.05	−0.18
6500.....	7.5	+0.46	+0.30	+1.17	+0.31	+0.22	+0.03	−0.18
7000.....	7.5	+0.39	+0.24	+0.97	+0.28	+0.19	+0.01	−0.20
7500.....	7.5	+0.34	+0.19	+0.78	+0.26	+0.15	−0.01	−0.22
8000.....	7.5	+0.30	+0.13	+0.61	+0.27	+0.12	−0.03	−0.25
8500.....	7.5	+0.28	+0.06	+0.45	+0.31	+0.09	−0.04	−0.27
9000.....	7.5	+0.26	−0.05	+0.29	+0.40	+0.07	−0.06	−0.30
9500.....	7.5	+0.24	−0.18	+0.15	+0.54	+0.04	−0.08	−0.33
10000.....	7.5	+0.22	−0.33	+0.02	+0.70	+0.02	−0.10	−0.37
4000.....	8.0	+0.99	+0.63	+1.31	+0.62	−0.14	−0.12	−0.29
4250.....	8.0	+0.94	+0.60	+1.58	+0.60	−0.04	−0.06	−0.32
4500.....	8.0	+0.88	+0.56	+1.75	+0.56	+0.08	−0.02	−0.32
4750.....	8.0	+0.83	+0.52	+1.83	+0.53	+0.18	+0.02	−0.31
5000.....	8.0	+0.77	+0.49	+1.83	+0.49	+0.24	+0.06	−0.27
5250.....	8.0	+0.72	+0.45	+1.77	+0.46	+0.26	+0.08	−0.24
5500.....	8.0	+0.66	+0.42	+1.65	+0.42	+0.26	+0.08	−0.21
6000.....	8.0	+0.56	+0.36	+1.40	+0.36	+0.23	+0.06	−0.17
6500.....	8.0	+0.47	+0.30	+1.17	+0.31	+0.21	+0.03	−0.17
7000.....	8.0	+0.40	+0.25	+0.97	+0.27	+0.18	+0.01	−0.20
7500.....	8.0	+0.34	+0.20	+0.79	+0.25	+0.15	−0.01	−0.23
8000.....	8.0	+0.31	+0.15	+0.62	+0.25	+0.12	−0.02	−0.26
8500.....	8.0	+0.28	+0.09	+0.46	+0.27	+0.10	−0.04	−0.29
9000.....	8.0	+0.26	+0.01	+0.32	+0.32	+0.07	−0.05	−0.32
9500.....	8.0	+0.25	−0.09	+0.18	+0.41	+0.05	−0.07	−0.36
10000.....	8.0	+0.24	−0.21	+0.06	+0.54	+0.03	−0.08	−0.39
4000.....	8.5	+0.97	+0.61	+1.04	+0.60	−0.20	−0.16	−0.22
4250.....	8.5	+0.92	+0.58	+1.34	+0.58	−0.11	−0.09	−0.26
4500.....	8.5	+0.87	+0.55	+1.54	+0.55	+0.00	−0.05	−0.28
4750.....	8.5	+0.81	+0.52	+1.66	+0.52	+0.11	−0.02	−0.27
5000.....	8.5	+0.76	+0.48	+1.71	+0.49	+0.19	+0.02	−0.25
5250.....	8.5	+0.71	+0.45	+1.69	+0.45	+0.23	+0.06	−0.23
5500.....	8.5	+0.66	+0.42	+1.61	+0.42	+0.24	+0.07	−0.20
6000.....	8.5	+0.56	+0.36	+1.38	+0.36	+0.22	+0.06	−0.16
6500.....	8.5	+0.47	+0.30	+1.16	+0.31	+0.20	+0.03	−0.17
7000.....	8.5	+0.40	+0.25	+0.96	+0.27	+0.18	+0.01	−0.19
7500.....	8.5	+0.35	+0.21	+0.79	+0.24	+0.15	−0.01	−0.23
8000.....	8.5	+0.31	+0.16	+0.63	+0.23	+0.12	−0.02	−0.27
8500.....	8.5	+0.28	+0.11	+0.48	+0.24	+0.10	−0.04	−0.31
9000.....	8.5	+0.26	+0.05	+0.34	+0.27	+0.07	−0.05	−0.35
9500.....	8.5	+0.25	−0.02	+0.21	+0.32	+0.05	−0.06	−0.38
10000.....	8.5	+0.24	−0.12	+0.09	+0.41	+0.03	−0.07	−0.42

Tables 1–3 contain the broadband color indices for a subsample of our model grid including the pure hydrogen and pure helium models, as well as models at log $g = 8.0$ and mixed H/He compositions. Colors are defined in the Johnson system for B and V and the Cousins system for R and I. Although the JHK bandpasses from Bessel & Brett (1988) are on the Johnson-Glass system, the colors in Tables 1–3 are preferably given on the Carnegie image tube (CIT) system using the transformation equations of Leggett (1992, § A2.2). We also provide bolometric corrections (BCs) for each model following the prescription of Wesemael et al. (1980).

Figure 15 illustrates the ($B-V$, $V-K$) two-color diagram for models with various values of $T_{\rm eff}$, log g, and N(He)/N(H). In such a diagram, the pure hydrogen and pure helium sequences are well separated except in a small region around 4500 K (pure H) and 5300 K (pure He). In this region of the diagram, however, the infrared colors of pure hydrogen and pure helium models differ significantly (see Tables 1 and 3). The results of Figure 15 are in good qualitative agreement with those of Mould & Liebert (1978, Fig. 3), although both sets of colors differ quantitatively. Most noteworthy is the temperature at which the turnover occurs in the pure hydrogen models. In the Mould & Liebert models, the models with the largest values of $V-K$ correspond to $T_{\rm eff} \sim 5300$ K at log $g = 8.0$, while in our models, the turnover occurs at cooler effective temperatures ($T_{\rm eff} \sim 4800$ K).

We also show the location of the pure helium models of Kapranidis (1985) at $T_{\rm eff} = 4000$ and 4500 K, as well as the $T_{\rm eff} = 4500$ K FGVH model calculated in this analysis. These models are in fairly good agreement with each other, a result which is not too surprising since both calculations are based on comparable models of pressure ionization (see Fig. 10). The

TABLE 2

BROADBAND COLOR INDICES OF THE log $g = 8.0$ MIXED H/He MODELS

$T_{\rm eff}$ (K)	log y[a]	$B-V$	$V-R$	$V-K$	$R-I$	$J-H$	$H-K$	BC(V)
4000	−1.0	+0.98	+0.62	+1.05	+0.61	−0.20	−0.21	−0.24
4250	−1.0	+0.93	+0.59	+1.38	+0.59	−0.09	−0.12	−0.28
4500	−1.0	+0.87	+0.56	+1.60	+0.56	+0.03	−0.07	−0.30
4750	−1.0	+0.82	+0.52	+1.72	+0.53	+0.14	−0.02	−0.29
5000	−1.0	+0.76	+0.49	+1.77	+0.49	+0.22	+0.03	−0.27
5250	−1.0	+0.71	+0.45	+1.73	+0.46	+0.25	+0.07	−0.24
5500	−1.0	+0.66	+0.42	+1.64	+0.42	+0.25	+0.08	−0.21
6000	−1.0	+0.56	+0.36	+1.39	+0.36	+0.23	+0.06	−0.17
6500	−1.0	+0.47	+0.30	+1.16	+0.31	+0.21	+0.03	−0.17
7000	−1.0	+0.40	+0.25	+0.96	+0.27	+0.18	+0.01	−0.20
7500	−1.0	+0.34	+0.20	+0.78	+0.25	+0.15	−0.01	−0.23
8000	−1.0	+0.31	+0.15	+0.62	+0.24	+0.12	−0.02	−0.26
8500	−1.0	+0.28	+0.10	+0.47	+0.26	+0.10	−0.04	−0.30
9000	−1.0	+0.26	+0.02	+0.32	+0.31	+0.07	−0.05	−0.33
9500	−1.0	+0.25	−0.07	+0.19	+0.39	+0.05	−0.07	−0.36
10000	−1.0	+0.24	−0.18	+0.06	+0.51	+0.03	−0.08	−0.40
4000	0.0	+0.93	+0.58	−0.16	+0.56	−0.40	−0.65	−0.07
4250	0.0	+0.88	+0.56	+0.32	+0.55	−0.31	−0.53	−0.13
4500	0.0	+0.83	+0.53	+0.74	+0.53	−0.20	−0.39	−0.17
4750	0.0	+0.79	+0.50	+1.06	+0.51	−0.07	−0.27	−0.20
5000	0.0	+0.74	+0.47	+1.29	+0.48	+0.06	−0.18	−0.21
5250	0.0	+0.69	+0.44	+1.44	+0.45	+0.16	−0.07	−0.20
5500	0.0	+0.65	+0.41	+1.49	+0.42	+0.21	+0.01	−0.19
6000	0.0	+0.55	+0.35	+1.36	+0.36	+0.22	+0.05	−0.17
6500	0.0	+0.46	+0.30	+1.14	+0.31	+0.19	+0.03	−0.17
7000	0.0	+0.39	+0.25	+0.94	+0.27	+0.17	+0.01	−0.20
7500	0.0	+0.34	+0.21	+0.76	+0.24	+0.14	−0.01	−0.23
8000	0.0	+0.31	+0.16	+0.60	+0.23	+0.11	−0.02	−0.27
8500	0.0	+0.28	+0.11	+0.45	+0.23	+0.09	−0.03	−0.31
9000	0.0	+0.26	+0.05	+0.32	+0.26	+0.06	−0.05	−0.35
9500	0.0	+0.25	−0.03	+0.19	+0.33	+0.04	−0.06	−0.39
10000	0.0	+0.24	−0.12	+0.07	+0.42	+0.02	−0.07	−0.43
4000	1.0	+0.87	+0.53	−1.43	+0.46	−0.46	−1.01	+0.09
4250	1.0	+0.83	+0.51	−1.02	+0.48	−0.49	−0.92	+0.04
4500	1.0	+0.78	+0.49	−0.62	+0.47	−0.45	−0.83	+0.00
4750	1.0	+0.74	+0.46	−0.26	+0.46	−0.39	−0.73	−0.04
5000	1.0	+0.69	+0.44	+0.08	+0.44	−0.30	−0.61	−0.07
5250	1.0	+0.66	+0.42	+0.39	+0.42	−0.17	−0.50	−0.09
5500	1.0	+0.62	+0.39	+0.66	+0.39	−0.04	−0.38	−0.11
6000	1.0	+0.55	+0.35	+1.04	+0.35	+0.12	−0.09	−0.13
6500	1.0	+0.45	+0.29	+1.02	+0.30	+0.14	+0.03	−0.15
7000	1.0	+0.39	+0.24	+0.83	+0.25	+0.12	+0.02	−0.18
7500	1.0	+0.33	+0.20	+0.65	+0.22	+0.09	+0.00	−0.22
8000	1.0	+0.29	+0.16	+0.50	+0.20	+0.07	−0.01	−0.27
8500	1.0	+0.26	+0.12	+0.36	+0.19	+0.05	−0.02	−0.32
9000	1.0	+0.24	+0.08	+0.23	+0.19	+0.03	−0.03	−0.37
9500	1.0	+0.23	+0.03	+0.12	+0.21	+0.01	−0.04	−0.42
10000	1.0	+0.22	−0.03	+0.02	+0.25	+0.00	−0.05	−0.47
4000	2.0	+0.86	+0.51	−1.59	+0.44	−0.42	−1.05	+0.13
4250	2.0	+0.81	+0.49	−1.29	+0.45	−0.50	−0.97	+0.08
4500	2.0	+0.76	+0.47	−0.98	+0.44	−0.50	−0.91	+0.05
4750	2.0	+0.72	+0.44	−0.67	+0.43	−0.47	−0.84	+0.02
5000	2.0	+0.67	+0.42	−0.32	+0.41	−0.39	−0.71	−0.01
5250	2.0	+0.64	+0.40	−0.04	+0.39	−0.29	−0.63	−0.04
5500	2.0	+0.60	+0.38	+0.25	+0.37	−0.15	−0.52	−0.06
6000	2.0	+0.52	+0.33	+0.72	+0.32	+0.05	−0.21	−0.09
6500	2.0	+0.44	+0.28	+0.83	+0.27	+0.10	−0.01	−0.12
7000	2.0	+0.37	+0.23	+0.70	+0.23	+0.08	+0.03	−0.15
7500	2.0	+0.31	+0.20	+0.53	+0.19	+0.06	+0.01	−0.19
8000	2.0	+0.27	+0.16	+0.38	+0.16	+0.04	+0.00	−0.24
8500	2.0	+0.23	+0.13	+0.25	+0.14	+0.02	−0.01	−0.29
9000	2.0	+0.20	+0.10	+0.14	+0.12	+0.01	−0.02	−0.35
9500	2.0	+0.17	+0.07	+0.03	+0.10	+0.00	−0.03	−0.41
10000	2.0	+0.15	+0.04	−0.06	+0.10	−0.02	−0.04	−0.47

[a] $y \equiv N({\rm He})/N({\rm H})$.

TABLE 3

BROADBAND COLOR INDICES OF THE PURE HELIUM MODELS

$T_{\rm eff}$ (K)	log g	$B-V$	$V-R$	$V-K$	$R-I$	$J-H$	$H-K$	BC(V)
4000.....	7.5	+1.69	+1.03	+3.47	+0.94	+0.34	+0.21	−1.17
4250.....	7.5	+1.53	+0.90	+2.99	+0.82	+0.29	+0.18	−0.87
4500.....	7.5	+1.37	+0.78	+2.58	+0.71	+0.25	+0.16	−0.61
4750.....	7.5	+1.21	+0.68	+2.23	+0.62	+0.22	+0.14	−0.42
5000.....	7.5	+1.06	+0.59	+1.93	+0.54	+0.20	+0.13	−0.27
5250.....	7.5	+0.93	+0.51	+1.68	+0.47	+0.18	+0.11	−0.16
5500.....	7.5	+0.81	+0.45	+1.48	+0.42	+0.16	+0.10	−0.10
6000.....	7.5	+0.62	+0.36	+1.16	+0.34	+0.13	+0.08	−0.04
6500.....	7.5	+0.50	+0.30	+0.92	+0.28	+0.11	+0.06	−0.05
7000.....	7.5	+0.41	+0.25	+0.73	+0.23	+0.08	+0.04	−0.08
7500.....	7.5	+0.34	+0.21	+0.57	+0.19	+0.07	+0.03	−0.13
8000.....	7.5	+0.28	+0.18	+0.44	+0.16	+0.05	+0.01	−0.19
8500.....	7.5	+0.24	+0.16	+0.32	+0.13	+0.03	+0.00	−0.26
9000.....	7.5	+0.19	+0.13	+0.21	+0.11	+0.02	−0.01	−0.33
9500.....	7.5	+0.16	+0.11	+0.13	+0.09	+0.01	−0.02	−0.41
10000.....	7.5	+0.13	+0.10	+0.04	+0.07	+0.00	−0.03	−0.50
4000.....	8.0	+1.58	+0.93	+3.20	+0.85	+0.33	+0.21	−0.98
4250.....	8.0	+1.42	+0.82	+2.78	+0.75	+0.29	+0.19	−0.71
4500.....	8.0	+1.26	+0.71	+2.43	+0.65	+0.26	+0.17	−0.51
4750.....	8.0	+1.11	+0.63	+2.12	+0.58	+0.23	+0.15	−0.35
5000.....	8.0	+0.98	+0.55	+1.86	+0.51	+0.20	+0.13	−0.23
5250.....	8.0	+0.86	+0.49	+1.64	+0.45	+0.18	+0.11	−0.15
5500.....	8.0	+0.76	+0.43	+1.45	+0.41	+0.16	+0.10	−0.10
6000.....	8.0	+0.60	+0.35	+1.16	+0.33	+0.13	+0.08	−0.05
6500.....	8.0	+0.49	+0.29	+0.93	+0.28	+0.11	+0.06	−0.06
7000.....	8.0	+0.40	+0.25	+0.74	+0.23	+0.09	+0.04	−0.09
7500.....	8.0	+0.34	+0.21	+0.58	+0.19	+0.07	+0.03	−0.14
8000.....	8.0	+0.28	+0.18	+0.44	+0.16	+0.05	+0.01	−0.20
8500.....	8.0	+0.24	+0.16	+0.32	+0.13	+0.03	+0.00	−0.26
9000.....	8.0	+0.20	+0.13	+0.22	+0.11	+0.02	−0.01	−0.33
9500.....	8.0	+0.16	+0.11	+0.13	+0.09	+0.01	−0.02	−0.41
10000.....	8.0	+0.13	+0.10	+0.04	+0.07	+0.00	−0.03	−0.50
4000.....	8.5	+1.44	+0.84	+2.98	+0.78	+0.33	+0.22	−0.81
4250.....	8.5	+1.29	+0.74	+2.62	+0.69	+0.29	+0.19	−0.60
4500.....	8.5	+1.14	+0.65	+2.31	+0.61	+0.26	+0.17	−0.43
4750.....	8.5	+1.02	+0.58	+2.04	+0.55	+0.23	+0.15	−0.31
5000.....	8.5	+0.90	+0.52	+1.81	+0.49	+0.21	+0.13	−0.22
5250.....	8.5	+0.80	+0.47	+1.61	+0.44	+0.19	+0.12	−0.15
5500.....	8.5	+0.72	+0.42	+1.44	+0.40	+0.17	+0.10	−0.10
6000.....	8.5	+0.58	+0.35	+1.16	+0.33	+0.14	+0.08	−0.07
6500.....	8.5	+0.48	+0.29	+0.93	+0.28	+0.11	+0.06	−0.07
7000.....	8.5	+0.40	+0.25	+0.74	+0.23	+0.09	+0.04	−0.10
7500.....	8.5	+0.34	+0.21	+0.58	+0.19	+0.07	+0.03	−0.14
8000.....	8.5	+0.28	+0.18	+0.44	+0.16	+0.05	+0.01	−0.20
8500.....	8.5	+0.24	+0.16	+0.32	+0.13	+0.03	+0.00	−0.26
9000.....	8.5	+0.20	+0.13	+0.22	+0.11	+0.02	−0.01	−0.33
9500.....	8.5	+0.16	+0.11	+0.13	+0.09	+0.01	−0.02	−0.42
10000.....	8.5	+0.13	+0.10	+0.05	+0.07	+0.00	−0.03	−0.50

inclusion of a realistic model of pressure ionization, on the other hand, yields $B-V$ and $V-K$ colors that are $\sim$0.3 mag redder at $T_{\rm eff}$ = 4500 K. We note that the models of Mould & Liebert (1978; not shown here) are likely to possess even larger electron densities than those of Kapranidis or FGVH since Mould & Liebert have assumed a finite metallicity ($Z/Z_{\odot} = 10^{-5}$). Therefore, their predicted color indices are even bluer. For instance, the objects shown as filled triangles in Mould & Liebert (1978, Fig. 3) have been interpreted as evidence for line blanketing at blue wavelengths; the observed colors were apparently too red in $B-V$ to match any of their model sequences. They note, however, that an alternative explanation for this observed blue deficiency could be that the stars have atmospheres dominated by Rayleigh scattering, an interpretation they rejected on the basis of the earlier work of Böhm et al. (1977). Our new model atmosphere calculations provide a natural explanation for the existence of these objects in the context of pure helium compositions.

Perhaps of greater interest is the effect of mixed H/He compositions in the two-color diagram shown in Figure 15. A small value of N(He)/N(H) = 0.1 affects the colors only marginally, an effect which can be compensated, to some extent, by increasing the log g value of a pure hydrogen model; this behavior is reminiscent of the effects of helium on the Balmer line profiles and Strömgren color indices of cool DA white dwarfs, as discussed in detail by Bergeron et al. (1991). At much higher helium abundances, however, the collision-induced absorptions by H_2 due to collisions with helium strongly affect

the emergent fluxes at K and, consequently, the $V-K$ color indices.[5] Such cool, helium-rich objects can easily be detected in this diagram. Interestingly enough, the preliminary results of the spectroscopic and photometric survey of Bergeron et al. (1994), and summarized in Ruiz et al. (1993), reveal no such objects in a sample of over 70 cool DC and DA white dwarfs, with the exception of LHS 1126, marked in Figure 15 and analyzed in Bergeron et al. (1994b). The astrophysical consequences of these results will await for a more detailed analysis of the observations with the models developed in this paper.

[5] Eventually, for extremely large helium abundances, the photometric sequences will move back toward those of the pure helium models. Model atmospheres with such large helium abundances where this phenomenon occurs have not been calculated in this analysis, however.

The study of Bergeron et al. (1994) should ultimately confirm the relevance of our model calculations to the study of cool white dwarf atmospheres. In turn, the results will shed some light on the chemical compositions and evolution of white dwarf stars at the end of the cooling sequence.

We are grateful to G. Fontaine and A. Borysow for enlightening discussions and to P. Lenzuni for providing us with unpublished material. This work was supported in part by the NSERC Canada, the Fund FCAR (Québec), NSF grant AST 89-10780, and NASA grant HF-1051.01-93A from the Space Telescope Science Institute, which is operated by the Association of Universities for Research in Astronomy, Inc., under NASA contract NAS 5-26555.

REFERENCES

Bergeron, P., Ruiz, M.-T., & Leggett, S. K. 1992, ApJ, 400, 315
———. 1994a, in preparation
Bergeron, P., Ruiz, M.-T., Leggett, S. K., Saumon, D., & Wesemael, F. 1994b, ApJ, 423, 456
Bergeron, P., Wesemael, F., & Fontaine, G. 1991, ApJ, 367, 253
———. 1992, ApJ, 387, 288
Bessel, M. S. 1990, PASP, 102, 1181
Bessel, M. S., & Brett, J. M. 1988, PASP, 100, 1134
Böhm, K. H., Carson, T. R., Fontaine, G., & Van Horn, H. M. 1977, ApJ, 217, 521
Borysow, A., & Frommhold, L. 1989, ApJ, 341, 549
———. 1990, ApJ, 348, L41
Borysow, A., Frommhold, L., & Moraldi, M. 1989, ApJ, 336, 495
Borysow, J., Trafton, L., Frommhold, L., & Birnbaum, G. 1985, ApJ, 296, 644
Carson, T. R. 1977, unpublished
Carson, T. R., Mayers, D. F., & Stibbs, D. W. N. 1968, MNRAS, 140, 483
Fontaine, G., Graboske, H. C., Jr., & Van Horn, H. M. 1977, ApJS, 35, 293 (FGVH)
Fontaine, G., Villeneuve, B., & Wilson, J. 1981, ApJ, 243, 550,
Fontaine, G., & Wesemael, F. 1991, in Evolution of Stars: The Stellar Abundance Connection, ed. G. Michaud & A. Tutukov (Dordrecht: Reidel), 421
Hayes, D. S. 1985, in IAU Symp. 111, Calibration of Fundamental Stellar Quantities, ed. D. S. Hayes, L. E. Pasinetti, & A. G. Davis Philip (Dordrecht; Reidel), 225.
Hummer, D. G., & Mihalas, D. 1988, ApJ, 331, 794
Kapranidis, S. 1982, Ph.D. thesis, Univ. of Washington
———. 1983, ApJ, 275, 342
Kapranidis, S. 1985, ApJ, 294, 634
Koester, D. 1991, in Evolution of Stars: The Stellar Abundance Connection, ed. G. Michaud & A. Tutukov (Dordrecht: Reidel), 435
Leggett, S. K. 1992, ApJS, 82, 351
Lenzuni, P., Chernoff, D. F., & Salpeter, E. E. 1991, ApJS, 76, 759
Liebert, J. 1991, in Evolution of Stars: The Stellar Abundance Connection, ed. G. Michaud & A. Tutukov (Dordrecht: Reidel), 411
Linsky, J. L. 1969, ApJ, 156, 989
Mountain, C. M., Leggett, S. K., Selby, M. J., Blackwell, D. E., & Petford, A. D. 1985, A&A, 151, 399
Mould, J., & Liebert, J. 1978, ApJ, 226, L29
Nellis, W. J., Holmes, N. C., Mitchell, A. C., Trainor, R. J., Governo, G. K., Ross, M., & Young, D. A. 1984, Phys. Rev. Lett., 53, 1248
Patch, R. W. 1971, J. Quant, Spectrosc. Rad. Trans., 11, 1331
Ruiz, M.-T., Bergeron, P., & Leggett, S. K. 1993, in White Dwarfs: Advances in Observation and Theory, ed. M. A. Barstow (Dordrecht: Kluwer, 245
Saumon, D., Bergeron, P., Lunine, J. I., Hubbard, W. B., & Burrows, A. 1994a, ApJ, 424, 333
Saumon, D., & Chabrier, G. 1992, Phys. Rev. A, 46, 2084
Saumon, D., Chabrier, G., & Van Horn, H. M. 1994b, ApJS, submitted (SCVH)
Shipman, H. L. 1977, ApJ, 213, 138
Wesemael, F., Auer, L. H., Van Horn, H. M., & Savedoff, M. P. 1980, ApJ, 43, 159
Wickramasinghe, D. T., Allen, D. A., & Bessel, M. S. 1982, MNRAS, 198, 473
Zheng, C., & Borysow, A. 1995, ApJ, 441, 960